

## The evolution of pore pressure fields around standard and ball penetrometers: influence of penetration rate

Derek Elsworth<sup>\*,†</sup>

*Energy and Mineral Engineering and Energy Institute, Penn State University, University Park, Pennsylvania, U.S.A.*

### SUMMARY

Rate effects are examined in the steady pore pressure distribution induced as a result of penetration of standard and ball penetrometers. The incompressible flow field, which develops around the penetrometer is used to define the approximate soil velocity field local to the penetrometer tip. This prescribes the Lagrangian framework for the migration of the fluid saturated porous medium, defining the advection of induced pore pressures relative to the pressure-monitoring locations present on the probe face. In two separate approaches, different source functions are used to define the undrained pore fluid pressures developed either (i) on the face of the penetrometer or (ii) in the material comprising the failure zone surrounding the penetrometer tip. In the first, the sources applied at the tip face balance the volume of fluid mobilized by the piston displacement of the advancing penetrometer. Alternately, a fluid source distribution is evaluated from plasticity solutions and distributed throughout the tip process zone: for a standard penetrometer, the solution is for the expansion of a spherical cavity, and for the ball penetrometer, the solution is an elastic distribution of stresses conditioned by the limit load embedded within an infinite medium. For the standard penetrometer, the transition from drained to undrained behavior occurs over about two orders of magnitude in penetration rate for pore pressures recorded at the tip (U1) and about two-and-a-half orders of magnitude for the shoulder (U2). This response is strongly influenced by the rigidity of the soil and slightly influenced by the model linking induced total stresses to pore pressures. For the ball penetrometer, the transition from drained to undrained behavior also transits two-and-a-half orders of magnitude in penetration rate, although it is offset to higher dimensionless penetration rates than for standard penetration. Copyright © 2012 John Wiley & Sons, Ltd.

Received 9 October 2009; Revised 27 July 2010; Accepted 9 June 2012

KEY WORDS: penetrometer; permeability; Lagrangian; rate effects; pore pressure; ball penetrometers

### 1. INTRODUCTION

The cone penetration test (uCPT) is a widely utilized tool for characterizing soils and their geotechnical properties *in situ*. The recovered data can be used to assess the nature and sequence of the subsurface strata, together with their mechanical and transport properties. The current standard for the uCPT test involves the steady penetration at 2 cm/s by a 35.7 mm diameter cone (10-cm<sup>2</sup> cross-sectional area), with a 60° inter-apical angle, and the collection of continuous profiles of end-bearing stress, sleeve-frictional stress, and induced pore fluid pressure. Pore pressures are typically measured at the cone tip, the cone shoulder, or along the shaft, and these measurements are known to differ, because of both material nonlinearities and the physical geometry of the penetrometer and the advecting soil. Together with the end-bearing and sleeve frictional stresses, pore pressures are used to determine mechanical and transport properties of the soil [1].

\*Correspondence to: Derek Elsworth, Energy and Mineral Engineering and Energy Institute, Penn State University, University Park, PA 16802, U.S.A.

†E-mail: elsworth@psu.edu

Empirical correlations have been developed for qualitatively defining soil types [2] along with analytical methods to understand the mechanics of the processes involved with penetrometer insertion, which primarily involve the strain and pressure fields that develop around the cone during advancement. These analytical methods can be divided into two broad classes of models; static and migrating. Static models mainly relate to cavity expansion results for spherical [3] and cylindrical [4] geometries. These models have been shown to be capable of incorporating frictional behavior [5] and shear-induced pore pressures [6]. They have been applied to define the initial undrained distributions of pore pressure and their subsequent dissipation [4, 6, 7] and have been used in determining the hydraulic diffusivity of soils. Although a limitation exists for cavity expansion models to reproduce pore-pressure fields that result at the cone tip, the more pressing limitation is the inability to accommodate the precise tip geometry of the penetrometer and the role of rate-effects on the resulting response. Pore-pressure fields that develop around a steady penetrating cone have been shown to be strongly dependent on the shape of the cone tip and the degree of taper [8]. Thus, the locations of the pressure-sensing element inlets are important [9]. These limitations on using cavity expansion methods to represent these facets make their use in data reduction problematic.

Migrating models are those that accommodate the non-inertial dynamic effects of the moving penetrometer tip. Important criteria are as follows: (i) accurately determining the evolving tip local strain field, and (ii) accommodating the partial drainage conditions by allowing simultaneous pore-pressure generation and dissipation. Different models have been shown to meet these requirements to varying degrees. The tip local strain fields may be determined from considerations of kinematic failure mechanisms [10, 11] and by considering steady plastic flow [12, 13]. Appropriate pore-pressure parameters can be used to determine the instantaneous pore-pressure distributions [14, 15]. Strain path analyses [16] circumvent many of the complexities involved in defining the large strain field, where slight variations in the evolving strain distribution induced at the tip are considered of secondary importance to the intense impacts of material nonlinearity. Instead, an approximate solution is sought to the mechanical problem, neglecting rigorous solution of the equilibrium equations but providing an evaluation of strain distributions to the applied displacement (or displacement rate) boundary conditions. This procedure is shown to provide adequate predictions of the distribution of undrained pore pressure generation [17, 8], adequately incorporating cone geometry effects, and may be applied equally to complex and relatively straightforward [18] material models.

Dislocation-based methods [19–21] provide an alternative to the strain-path methods and enable both the undrained and partially drained behaviors to be accommodated, along with simultaneous fluid pressure generation and dissipation. The main limitations of these models are that general pseudo-elastic material behavior is used, which negates the development of a true tip local process zone. Also, the analyses are for moving point dislocations within the poroelastic medium and do not adequately represent the influence of the tip geometry and its finite size on pressure generation. Despite these limitations, the penetration induced fluid pressure response evaluated from the dislocation analysis closely matches the undrained behavior observed [17] and replicated by other methods [8, 18] and are not restricted to undrained behavior alone.

The following presents a first analysis for conical and ball penetrometers moving within a porous medium using a Lagrangian representation where evolution of pore pressures local to the tip is recovered from a solution for undrained failure. This enables the influence of the finite size and true flow-field around the tip to be accommodated, together with the effects of fluid storage and release from storage during the initiation and arrest of penetration, including the effects of convective transport. This analysis supplements previous steady-state characterizations [22], which have proved useful in recovering profiles of permeability data from peak pore pressure magnitudes measured on-the-fly. This analysis addresses the anomaly between previously observed and calculated pore pressure magnitudes using the assumption of an amorphous tip, steady-state pressure buildup, and negligible fluid storage.

## 2. ANALYSIS OF FLUID PRESSURES IN AN ADVECTING FLOWFIELD

Prior results have represented the evolution of the pore pressure field by injecting an equivalent volume of fluid into the flowing stream of soil as it moves past the penetrometer tip. This fluid injection rate

corresponds to the insertion rate of the penetrometer, and the solution can be shown to be equivalent to models represented by a moving point dislocation [19]. This method has been applied to both infinitesimal [21] and finite size [23] penetrometers where the distribution of fluid injection around the boundary is prescribed by the local geometry. In this work, we extend this approach to distribute the injected volume throughout the tip process zone; the injected fluid volume is defined by the tip-local failure mechanism. This yields a more accurate representation of the evolving pore pressure field local to the tip and allows an analysis of penetration rate effects.

2.1. Fluid pressure field

For this distributed source, the evolving pore pressure field may be represented by the governing equation for fluid flow within an advecting medium [24],

$$m_v \frac{\partial p}{\partial t} + m_v v_i \frac{\partial p}{\partial x_i} - \frac{\partial}{\partial x_i} \frac{k_i}{\mu} \frac{\partial p}{\partial x_i} - Q = 0 \tag{1}$$

where  $Q$  is a distributed flux within the body (not a boundary flux), with units of volume injected, per unit volume, per unit time (i.e.  $s^{-1}$ ) and positive for injection into the flow-field. The moving soil–fluid mixture has a volume compressibility,  $m_v$ , permeability,  $k_i$ , local velocity  $v_i$  in the  $i$ -th direction, and the pore fluid exists at pressure,  $p$ , and viscosity,  $\mu$ . The coordinates are  $x_i$ , and the behavior evolves over time,  $t$ . For the moving reference frame, the distributed flux may be defined by an apparent volume strain,  $\varepsilon_v$ , given by,

$$Q = \frac{D\varepsilon_v}{Dt} = \frac{\partial \varepsilon_v}{\partial t} + v_i \frac{\partial \varepsilon_v}{\partial x_i} \tag{2}$$

This distributed volumetric flux is the fluid volume made available by undrained incremental straining of the medium, and its redistribution in space is controlled by pressure diffusion. This redistribution is controlled by Equation (1) through fluid transport modulated by Darcy’s law and through release from storage modulated via  $m_v$ , hence, noting that for drained loading under constant total stresses, and where  $m_v$  represents the volumetric response as  $m_v = 1/K$  where  $K$  is the drained bulk modulus. Note that  $m_v$  in this use is not the constrained compressibility because the medium is free to expand laterally in the geometry selected. The modulus may be either the virgin compression modulus or the unload-reload modulus representing recompression to prior conditions, determined by preference. Thus, the fluid available for redistribution is

$$\varepsilon_v = \frac{1}{K} p^u = m_v p^u \tag{3}$$

Substituting Equation (3) into Equation (2), the result into Equation (1), and non-dimensionalizing by multiplying by  $a/U$ , where  $a$  is penetrometer radius and  $U$  is penetrometer velocity, yields the dimensionless expression

$$\frac{\partial P_D}{\partial t_D} + U_D \left( \frac{v_i}{U} \right) \frac{\partial P_D}{\partial x_D} - \frac{\partial}{\partial x_D} \frac{\partial P_D}{\partial x_D} + Q_D = 0 \tag{4}$$

noted in compact form for all dimensions  $x_i$  and with the steady form ( $\partial \varepsilon_v / \partial t = 0$ ) of the source function,  $Q_D$ , defined as

$$Q_D = \left( \frac{v_i}{U} \right) \frac{\partial (m_v p^u)}{\partial x_D} = \left( \frac{v_i}{U} \right) \frac{\partial (P^u_D)}{\partial x_D} \tag{5}$$

The remaining terms are of non-dimensional pressure,  $P_D$ ,

$$P_D = \frac{k_i (p - p_s)}{\mu Ua} \tag{6}$$

non-dimensional penetration rate,  $U_D$ ,

$$U_D = \frac{Ua}{C_v} \quad (7)$$

non-dimensional time,  $t_D$ ,

$$t_D = \frac{C_v t}{a^2} \quad (8)$$

and for a non-dimensional coordinate system,  $x_D$ ,

$$x_D = x_i/a. \quad (9)$$

The dimensionless pressure is defined in terms of the static pressure,  $p_s$ , and measured pressure,  $p$ , and the penetrometer velocity  $v_1 = U$  and with a normalizing length defined by the penetrometer radius,  $a$ . Similarly, nondimensional penetration rate and pressure-diffusive time are conditioned by consolidation coefficient  $C_v$ , which is in turn a function of permeability and coefficient of volume compressibility as  $k = C_v m_v$ .

Similarly, the convective boundary conditions to the system may be cast in non-dimensional form, as

$$Q_D^b = -\frac{\partial P_D}{\partial x_D} + U_D \left( \frac{v_i}{U} \right) P_D; \quad P_D = P_{D\text{defined}} \quad (10)$$

where  $Q_D^b = q_i/U$ .

Additionally, if the magnitude of the fluid volumetric source term,  $m_v p^u$ , may be determined, then the evolving water pressure distribution in the moving reference frame may also be recovered. This pressure distribution must satisfy two end-member conditions: it must return the initial undrained prescribed pressure distribution at high penetration rates and must approach zero-induced pressure as the penetration rate approaches zero (drained loading). An alternate and separate requirement is that fluid mass must be conserved, and the fluid volume 'injected' into the flowing soil mass must be equivalent to the volume rate of penetrometer insertion.

## 2.2. Soil flow-field

Separate from the pressure diffusion equation, the overall flow-field of the fluid-saturated solid mixture must be defined. For this, the motion of the fluid–solid mixture is treated as the transport of a Newtonian fluid. The momentum balance and continuity equations for the flow of an incompressible fluid are

$$\rho_s \frac{\partial v_i}{\partial t} + \rho_s v_i \frac{\partial v_i}{\partial x_i} = \rho_s g \frac{\partial x_i}{\partial x_i} - \frac{\partial P}{\partial x_i} + \mu_s \frac{\partial}{\partial x_i} \frac{\partial v_i}{\partial x_i} \quad (11)$$

and

$$\frac{\partial v_i}{\partial x_i} = 0 \quad (12)$$

and are applied with the appropriate boundary conditions. The incompressible fluid here represents the moving soil–fluid mixture and has a mean density of  $\rho_s$  and viscosity  $\mu_s$ . Importantly, the fluid pressure of the mixture driving flow is the reduced fluid pressure  $P = \frac{1}{3}(\sigma_{11} + \sigma_{22} + \sigma_{33})$  and is used to condition flow at the desired velocity past the probe, in the far-field. For typical anticipated velocities, the convective accelerations and body forces are small in comparison to viscous effects, and the system may be adequately represented by steady Stokes flow for a non-inertial fluid. Thus, Equations (11) and (12) become

$$\frac{\partial P}{\partial x_i} = \mu_s \frac{\partial}{\partial x_i} \frac{\partial v_i}{\partial x_i} \tag{13}$$

and

$$\frac{\partial v_i}{\partial x_i} = 0 \tag{14}$$

or  $\nabla P = \mu \nabla^2 \mathbf{v}$  and  $\nabla \cdot \mathbf{v} = 0$ . This yields directly, for arbitrary penetrometer geometries, a flow field for an incompressible fluid representing the soil-water mixture, which is analogous to that used in strain path models. The flow is assumed incompressible, although consolidation and local fluid exchange will occur. Because this model for flow of the soil-water mixture is used only to prescribe the flow vectors for the migrating consolidation equation (Equation (4)), this effect is anticipated to be minor.

2.3. Numerical solution

The resulting system of equations is solved in finite element format. The geometry is as shown in Figure 1 for both tapered and spherical penetrometers. The resulting equations for soil flow are the finite element representation of the Stokes equations (for Equations (13) and (14)) as the momentum balance component

$$\int_V \left[ \underbrace{\underline{a}^T D \underline{a}}_{\mu_s \frac{\partial}{\partial x_i} \frac{\partial v_i}{\partial x_i}} \mathbf{v} + \underbrace{\tilde{\underline{a}}^T m b P}_{\frac{\partial P}{\partial x_i}} = 0 \right] dV \tag{15}$$

and for the continuity requirement as

$$\int_V \left[ \underbrace{\underline{b}^T \underline{m}^T \underline{a}}_{\frac{\partial v_i}{\partial x_i}} \mathbf{v} = 0 \right] dV. \tag{16}$$

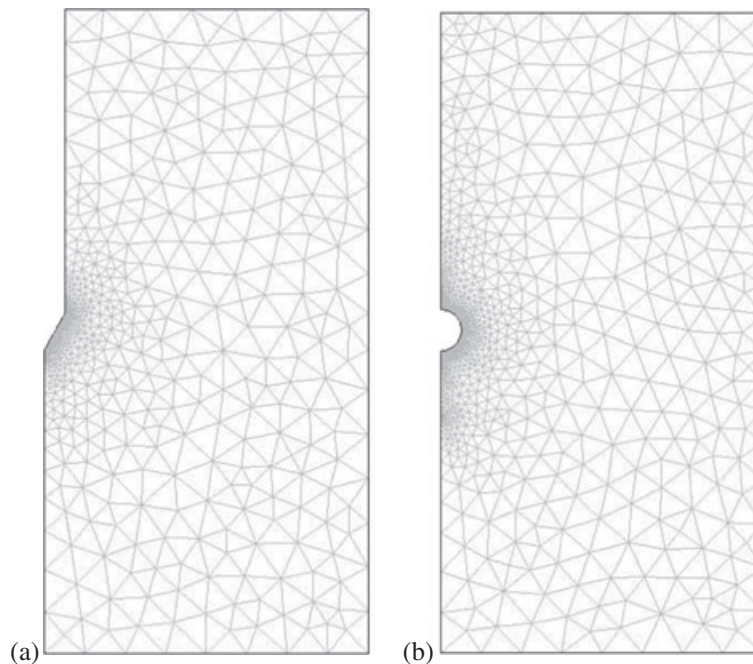


Figure 1. Meshes used for (a) standard and (b) ball penetrometers.

In this, vectors and matrices are underscored. The shape function vector is  $\underline{b}$ , and the derivatives of this link nodal pressures  $\underline{P}$  to pressure gradients  $\underline{P}_{,i}$  as  $\underline{P}_{,i} = \underline{\tilde{a}}\underline{P}$  and nodal velocities  $\underline{v}$  to velocity gradients  $\underline{v}_{,i}$  through  $\underline{v}_{,i} = \underline{a}\underline{v}$ . The matrix  $\underline{D}$  contains the constitutive relationship in terms of Newton's law of viscosity and for the three-dimensional case  $\underline{m}^T = [111000]$ . For the generation and transport of pore pressures within the advecting solid–fluid mixture (Equation (4)), the advection–diffusion equation becomes

$$\int_V \left[ \underbrace{\underline{b}^T \underline{b} \dot{\underline{P}}_D}_{\frac{\partial P_D}{\partial t}} - \underbrace{\underline{\tilde{a}}^T \underline{\tilde{a}} \underline{P}_D}_{\frac{\partial}{\partial x_D} \frac{\partial P_D}{\partial x_D}} - \underbrace{\underline{b}^T \underline{b} \underline{Q}_D}_{Q_D} + \underbrace{\underline{b}^T \underline{v}^T \underline{\tilde{a}} \underline{P}_D}_{U_D \left( \frac{v_i}{U} \right) \frac{\partial P_D}{\partial x_D}} = 0 \right] dV_D \quad (17)$$

where  $\underline{v}$  is the vector of local velocities,  $v_i$ , and the integration is completed over the dimensionless volume,  $dV_D = dx_D dy_D dz_D$ . It is important to note that the reduced pressure  $P$  that occurs in Equation (15) is the mean of the stresses in the solid–fluid mixture of the Stokes' equation. This solution is used to determine the spatial distributions of soil velocities,  $v_i$ , around the cone and is solved to return the desired penetration rate of the cone relative to the mean advection velocity,  $U$ , of the soil. The reduced pressure boundary conditions and viscosities are selected to return this required outcome. With the velocity field  $v_i$  known everywhere, then the generation and dissipation of pore fluid pressures,  $p$ , or their dimensionless counterpart,  $P_D$ , may then be determined from Equation (17). This solution is de-coupled.

The mesh is defined in the dimensionless coordinate system  $(x_D, r_D)$  and extends to 16 penetrometer-radii ( $a$ ) laterally and vertically relative to the mesh-centered penetrometer tips. The mesh is graded with element size a minimum close to the penetrometer face at  $\sim a/100$  and grades out to a maximum element size of  $\sim a$  at the outer boundaries. For the different geometries, this comprises a mesh of up to about 6000 triangular elements and 40 000 degrees of freedom for the axisymmetric problem. Triangular elements are used with quadratic shape functions  $\underline{b}$  applied to both the pressure and velocity conditions.

The moving soil is represented by Stokes' flow with slip conditions on the side boundaries (including the penetrometer faces) and reduced pressure conditions ( $P$ ) set to a unit differential between the domain base and top. The ratio of differential pressure to viscosity is adjusted to yield a mean unit vertical velocity within the far field, which is then scaled by  $U_D$  across the domain as input to the Lagrangian consolidation equation (Equation (4)). Note that the reduced pressure gradient is used to match the bulk motion of the soil–water mixture to the desired insertion rate ( $U$ ) of the penetrometer and is merely a scaling parameter. It is not related to the pore pressure,  $p$ .

The consolidating soil is represented by zero flux on the sides, null pressure on the base and a convective condition on the top. Boundary and interior conditions for the standard and ball penetrometers are prescribed in one of two ways. For the undrained analysis with a distributed process zone, they are described as an interior volumetric flux  $\underline{Q}_D$  prescribed according to Equations (20) and (21) for the standard cone or Equation (29) for the ball penetrometer (as discussed later). For the partially drained analysis, the boundary condition is prescribed as a surface flux  $\underline{Q}_D^b$  according to Equation (25) for the standard cone and Equation (31) for the ball penetrometer (also as discussed later).

### 3. PORE PRESSURE RESPONSE FOR PENETRATION GEOMETRIES

This approach is used to represent the evolution of pore pressures around the tip. The soil–water flow field is determined from the Newtonian viscous model of Equations (15) and (16). This defines the velocities of the soil everywhere within the system. We then use the solution for fluid flow within this advecting medium within Equation (17) to define the pore pressure distribution. This requires that we define the appropriate fluid source term,  $\underline{Q}_D$ , or Equation (5) to substitute into Equation (17).

The pore pressure generation and dissipation response for various tip geometries may be accommodated if the appropriate distributed source may be defined for the particular penetrometer. In this work, we compare two end-member cases for each of two probe geometries: a standard conical penetrometer and a ball penetrometer. The end-member cases are for undrained loading, where a plasticity solution is used to define interior undrained pore pressures and related volume fluxes, and a partially drained solution where an equivalent fluid injection is applied at the cone tip face. These examples are examined sequentially in the following.

3.1. Standard conical penetrometer

3.1.1. Undrained solution. The source term to represent the lower bound solution for the expansion of a spherical cavity may be described as  $P_D^u = m_v p^u$  as [25]

$$P_D^u = \frac{4}{3} m_v S_u \left[ \left( 1 + \ln \left( \frac{G}{S_u} \right) \right) - \frac{3}{2} (1 - A_f) + 3 \ln \left( \frac{a}{R} \right) \right]; \quad a < R < R_{\max} = a(G/S_u)^{1/3} \quad (18)$$

$$P_D^u = 0; \quad R > R_{\max} = a(G/S_u)^{1/3} \quad (19)$$

where  $S_u$  may be a cohesive or pseudo-frictional strength parameter,  $A_f$  is the Skempton pore pressure coefficient ( $B = 1$ ), for  $p^u = B\Delta\sigma_3 - A_f B(\Delta\sigma_1 - \Delta\sigma_3)$  and the cavity is of radius,  $a$ .

The bulk compressibility,  $m_v = 1/K$ , and drained shear modulus,  $G$ , are related as  $K = \frac{2(1+\nu)}{3(1-2\nu)} G = fG$ , leaving  $f = 4/3$  for  $\nu = 0.2$  and  $f = 5/3$  for  $\nu = 0.25$ . Substituting this into Equation (18) and non-dimensionalizing the length dimensions as  $r^2 = y^2 + z^2$ ,  $r_D = r/a$  and  $R_D^2 = x_D^2 + r_D^2$  results in

$$P_D^u = \frac{4}{3f} \frac{S_u}{G} \left[ \left( 1 + \ln \left( \frac{G}{S_u} \right) \right) - \frac{3}{2} (1 - A_f) + 3 \ln \left( \frac{1}{R_D} \right) \right]; \quad 1 < R_D < R_{D\max} = (G/S_u)^{1/3} \quad (20)$$

with the pressure null beyond this. Because the pressure at the outermost limit of the plastic zone is finite (Equation (20)), but null immediately beyond this, this infinite pressure gradient is ameliorated by setting a smooth transitional distribution of the undrained pressure within the initial portion of the elastic zone. This distribution is scaled with the exponent  $n$  as

$$P_D^u = \left[ P_D^u|_{R_D=R_{D\max}} \left( \frac{R_{D\max}}{R_D} \right)^n \right]; \quad R_D > R_{D\max} = (G/S_u)^{1/3} \quad (21)$$

to give a smooth pressure distribution in the transition across the elastic-plastic interface, so the derivatives in Equation (5) are both finite and well conditioned. For spherical cavity expansion, the exponent  $n = 3$  gives continuity of pressure gradient across the boundary and is used here.

3.1.2. Partially drained solution. For an axisymmetric flow system, with the medium moving at velocity,  $U$ , boundary conditions may be defined for the geometry of a blunt penetrometer, where the fluid is injected through a band around the curved surface of a cylinder of radius,  $a$ , and length,  $l$ , at velocity,  $q$ . The appropriate non-dimensional flux  $Q_D = q/U$  may be defined as

$$Q_D^{b \text{ CPT-Blunt}} = \frac{a}{2l} = \frac{1}{2l_D} \quad (22)$$

For a standard cone (Figure 2) where the tip is tapered at semi-inter-apical angle  $\theta$  and the taper exists over length  $l$ , then the injected fluid may be applied over the face of this tapered cone. For a coordinate system  $(\chi, r)$  centered on the tip, with  $\chi$  positive in the direction of increasing tip taper, the volume of the tapered tip displaced per unit length of travel is [21]

$$V = 2\pi \tan^2 \theta U \chi d\chi \quad (23)$$

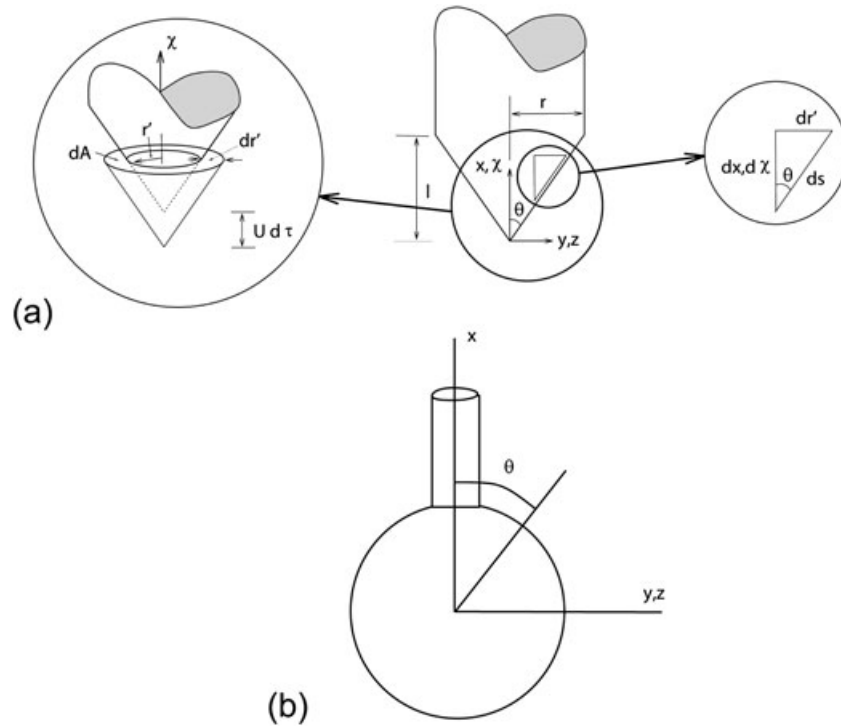


Figure 2. Prescribed tip geometries of (a) standard and (b) ball penetrometers.

where this volume is applied over the area of the cone surface, the velocity flux is given by  $q = V/2\pi a$  where  $a$  is the radius to the tapered face of the probe, where surface length  $dS$  is related to  $d\chi$  as  $d\chi = \tan \theta dS$ , to yield,

$$q = U \sin \theta dS \quad (24)$$

or  $U \sin \theta$  per unit length. This may be non-dimensionalized to give

$$Q_D^{b, CPT-Tapered} = \frac{q}{U} = \sin \theta \quad (25)$$

when applied normal to the tapered surface over the length of the tip  $l_D = 1/\tan \theta$ .

The numerical solution for a tapered geometry is compared against the analytical solution for a blunt penetrometer idealized as a moving point volumetric dislocation in a poroelastic medium [19]. The resulting pore pressure distribution is given as  $P_D = \frac{1}{4R_D} \exp[-\frac{1}{2}U_D(R_D - x_D)]$ . The geometries of the two systems are not identical, and the severity of the tip-local pressure gradients around the tip is a severe test for the numerical model. Nevertheless, the correspondence between numerical and analytical solutions, as illustrated in Figure 3, is adequate.

**3.1.3. Asymptotic pore pressure magnitudes.** For the assumptions embedded in each of the undrained and partially drained solutions, there are asymptotic magnitudes of non-dimensional pore pressure for idealized geometries. For the standard cone, this is a spherical cavity of radius  $a$  [23]. For the cavity expansion solution, and with  $A_f = 1/3$  to represent the elastic case of null pressure generation in shear, this yields at  $R_D = 1$  an undrained pressure of

$$P_D = \frac{4}{3} \frac{1}{f} \frac{Su}{G} \ln(G/Su) \quad (26)$$

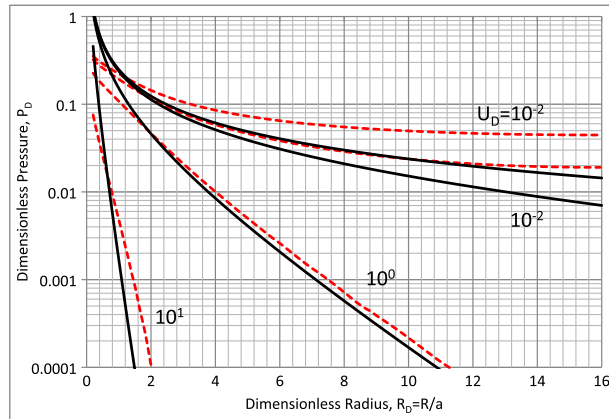


Figure 3. Comparison of numerical (dashed) solution for a tapered penetrometer against the analytical solutions (solid) for a moving point dilation [19] representing a blunt penetrometer. Radial solution at  $x_D=0$  for dislocation solution and horizontal radius at penetrometer tip for numerical solution.

and for the partially drained solution, neglecting storage (as  $m_v \rightarrow 0$ )  $P_D = 1/4$ [22]. These magnitudes may be used as both a check on the limiting magnitudes on predicted pore pressures, and as normalizing magnitudes to define normalized pore pressure magnitudes. These magnitudes are summarized for various magnitudes of  $G/Su$  in Table I.

**3.1.4. Results and discussion.** The undrained solution is used to evaluate the pressure response of a standard cone in steady penetration where partial drainage is conditioned by the penetration rate. The spherical cavity solution is centered on the cone axis, one radius behind the U1 position at the cone tip. The initial pore pressure field adjacent to the cone tip, prescribed as an interior condition, is shown in Figure 4(a) together with the streaklines identifying the path of the migrating soil around the tip. The form of the evolved pore pressure distribution  $(p - p_s)/K$  is also shown for dimensionless penetration rates  $U_D$  from 0.1 to 100. Apparent is the strengthening of the steady induced pore pressure field with an increase in penetration rate and the very slight elongation of the pore pressure field with increasing level of soil advection. On the fixed color scale of Figure 4, induced pore pressures are virtually absent at  $U_D < 0.1$ , representing drained behavior, and fully developed, representing undrained behavior for  $U_D > 10$ . This two orders of magnitude segment represents the partially drained regime.

The evolution of normalized pore pressures  $\Delta p/\Delta p_{max}$  at the tip (U1) and shoulder (U2) locations are shown as a function of penetration rate  $U_D = Ua/c$  in Figure 5. Similar to the results for the spatial distribution, these document the region of partial drainage to span about two-and-a-half orders of magnitude with a slight offset apparent for rigidity indices  $G/Su$  in the range 10–1000. All calculations are for pore pressure parameters in Equation (20) of  $B=1$  and  $A_f=1/3$ . In this configuration, the undrained pore pressure is equivalent to the minimum principal-induced stress  $p^u = B\Delta\sigma_3$ . The influence of variations in the pore pressure parameter  $A_f$  in the range  $-1/2$  to 1 are shown in Figure 6 to have only a small influence on the effects of insertion rate.

Table I. Asymptotic magnitudes of dimensionless pressures for standard and ball penetrometers.

$G/Su$	$P_D$ (Standard Penetrometer)	$P_D$ (Ball Penetrometer)
10	0.23	0.214
100	0.046	0.0214
1000	0.00691	0.00214
Partially drained	$\frac{1}{4}$	$\pm \frac{1}{2}$

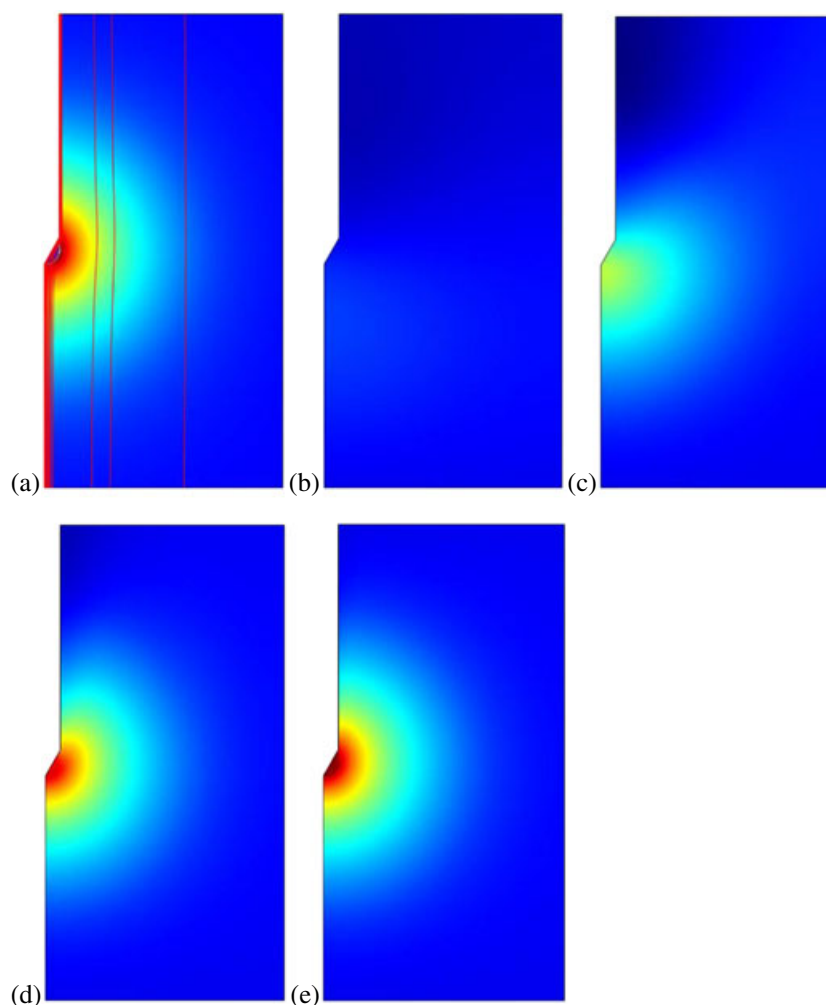


Figure 4. Contour plots of equivalent pore pressures around a standard penetrometer. Plots are for  $P_D U_D = (p - p_s)/K$  and at uniform color key for contours with hot representing highest pressure ( $P_D U_D = (p - p_s)/K = 7 \times 10^{-3}$ ). Individual frames are for (a) prescribed pressure field for undrained condition and streaklines for solid flowfield and for  $U_D = Ua/C_v$  magnitudes of (b) 0.1, (c) 1, (d) 10 and (e) 100, all for  $G/Su = 1000$ .

With these normalized responses representing a broad range of absolute-induced pressures, these same results ( $G/Su = 10; 100; 1000$ ) may be represented as pressures normalized with respect to bulk modulus as  $(p - p_s)/K$  as in Figure 7(a) or with respect to undrained shear strength as  $(p - p_s)/Su$  as in Figure 7(b). These magnitudes are for the U2 position on the shoulder and confirm the asymptotic magnitudes of induced pore pressures as dimensionless penetration rates increase above about 100. Absolute magnitudes of induced pore pressures increase with an increase in soil rigidity and conform to the undrained magnitudes prescribed at the cavity wall in Equation (26) and in Table I. Also shown are the magnitudes of pore fluid pressures predicted where injection from the penetrometer face is considered (Figure 7(a)). This behavior does not change with the soil stiffness, and the distribution with penetration rate is shown as an upper bound to the behaviors incorporating failure local to the tip.

Alternatively, the penetration-induced fluid may be normalized with respect to the effective vertical stress as  $(p - p_s)/\sigma_{v0}' = B_q Q_r$ . This representation has been used to examine the relationship between partially drained pore fluid pressures and *in situ* permeability [22, 23]. This conversion is not direct, as some assumption has to be made between the parameters  $G/Su$  and  $Su/\sigma_{v0}'$ . As a first-order estimate,

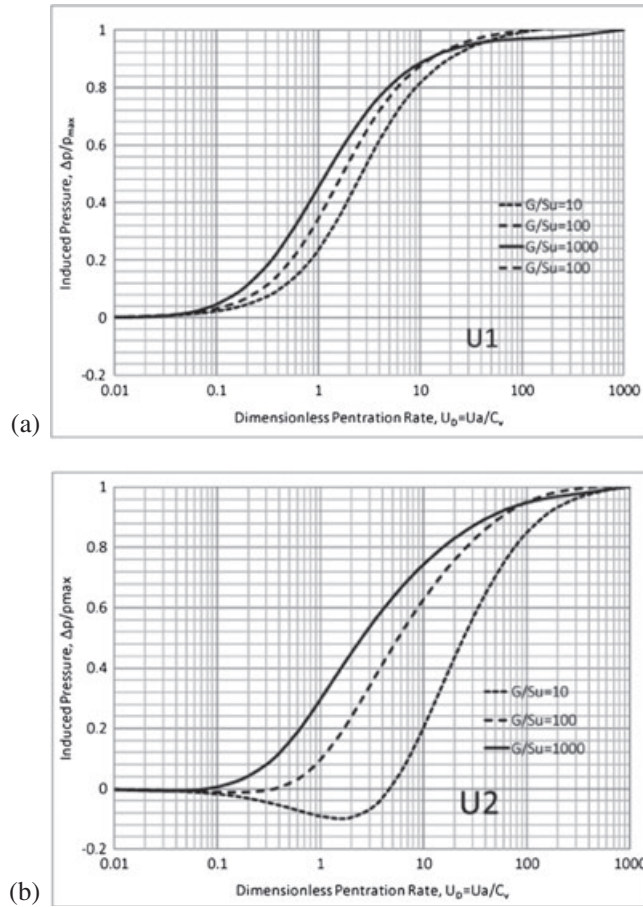


Figure 5. Variation of normalized pore pressures with insertion rate for a standard penetrometer for the (a) U1 (tip) and (b) U2 (shoulder) positions.  $G/Su$  in the range of 10, 100 and 1000. Pore pressures normalized relative to peak pore pressure for each magnitude of  $G/Su$ .

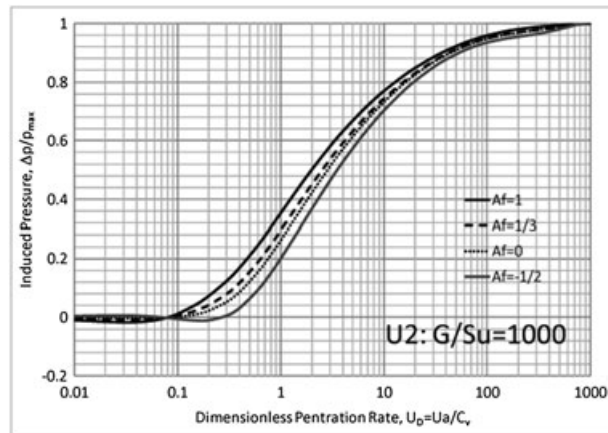
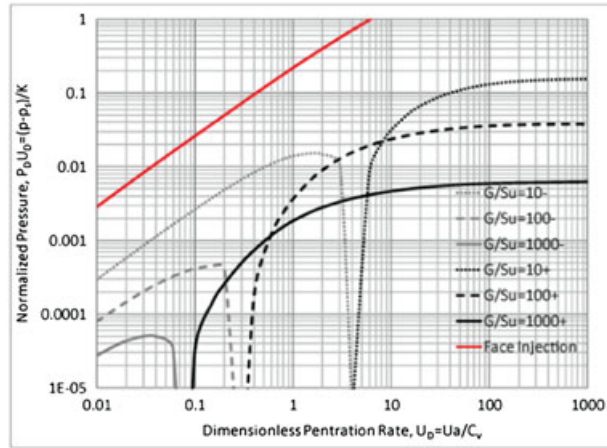
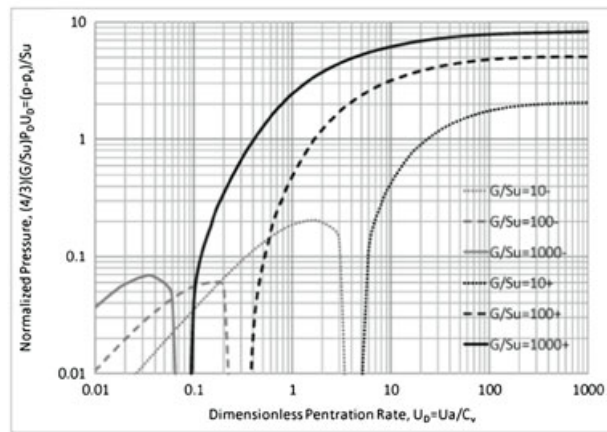


Figure 6. Variation of normalized pore pressures with insertion rate for a standard penetrometer for the U2 (shoulder) position for  $G/Su = 1000$  and magnitudes of  $A_f$  between  $-1/2$  and 1.

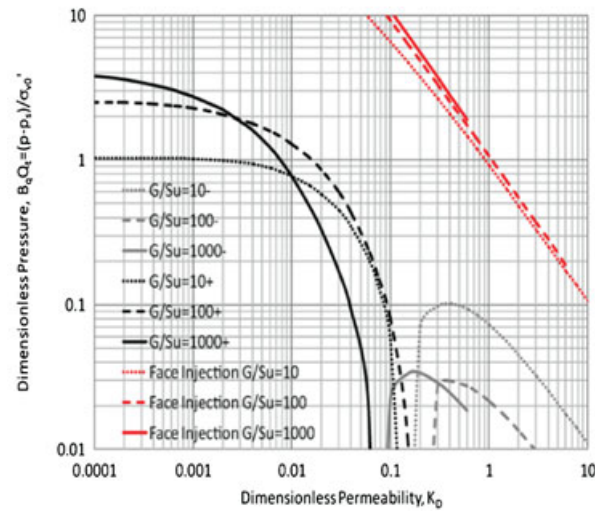
the plausible range is taken as  $0.3 < Su/\sigma_{v0}^l < 0.7$  and is taken as  $Su/\sigma_{v0}^l \approx 1/2$ . For this, substitution yields  $(p - p_s)/\sigma_{v0}^l = B_q Q_t = P_D U_D \frac{2}{3} \frac{G}{Su}$ . Similarly, a dimensionless permeability may be defined as [22]  $K_D = 4k\sigma_{v0}^l / \mu Ua \approx \frac{6}{U_D} \frac{Su}{G}$ , enabling the penetration-induced pressure to be



(a)



(b)



(c)

Figure 7. Variation in normalized pressures with dimensionless insertion rate ( $U_D$ ) for the U2 location on a standard penetrometer. Gray lines represent negative pore pressures as absolute. Induced pore fluid pressures are normalized with respect to (a) bulk modulus as  $(p - p_s)/K = 3(p - p_s)/4G$  and (b) undrained shear strength as  $(p - p_s)/Su$ . Alternately, assuming  $Su/\sigma'_{v0} \approx 1/2$  then the induced pressure may be represented as (c) cone metrics  $B_q Q_t = (p - p_s)/\sigma'_{v0}$  and plotted against non-dimensional permeability  $K_D = 4k\sigma'_{v0}/\mu Ua$ . Note vertical asymptotes are an artifact of plotting a trace of positive-turning-to-negative pressures on a log scale.

represented as a function of the dimensionless permeability, as shown in Figure 7(c). The behavior for both failure around the probe and for the face injection solution is shown. The undrained behavior on the left asymptotes to an upper limit and decreases sharply as the effects of partial drainage are felt. The transition to partial drainage is more rapid than for the face injection solution, which nonetheless bounds the observed failure responses. In the partially drained regime, the solutions involving the distributed source follow a similar trend, essentially overprinting in the range  $B_q Q_t < 1$ . This in turn may constitute a refined relationship between  $B_q Q_t$  and  $K_D$  as a predictive tool. Note that the vertical asymptotes on Figure 7 are an artifact of plotting a trace of positive-turning-to-negative pressures on a log scale.

3.2. Ball-tipped penetrometer

3.2.1. Undrained solution. Semi-analytical upper and lower bound solutions are available for the problem of a spherical penetrometer in a cohesive soil [26, 27]. These solutions converge to a limiting bearing capacity factor of  $N=11.42$  defined as the ratio of average penetration resistance pressure,  $q_u$ , to shear strength,  $S_u$ , as  $N=q_u/S_u$ . The undrained distribution of pore fluid pressures may be approximated by combining this limit load as a point force embedded within an infinite elastic medium to determine the change in mean stress and then relating this mean stress to change in pore pressures. The change in mean stress around an embedded point load of magnitude  $F$  (Kelvin solution) and for undrained conditions of zero volume change ( $\nu=0.5$ ) is defined as [28]

$$\left. \begin{aligned} \Delta\sigma_x &= -\frac{F}{4\pi R^5} \frac{3x^3}{R^2} \\ \Delta\sigma_r &= -\frac{F}{4\pi R^5} \frac{3xr^2}{R^2} \\ \Delta\sigma_\theta &= 0 \end{aligned} \right\} \Delta\sigma_m = \frac{1}{3}(\sigma_x + \sigma_r + \sigma_\theta) = -\frac{F}{4\pi R^2} \frac{x}{R} = -\frac{F}{4\pi R^2} \cos\theta \quad (27)$$

where the load is applied at ordinate  $(x, r)=(0, 0)$  along the  $x$ -axis but positive downward. Thus,  $R^2=x^2+r^2$  with  $\theta$  measured down from the  $x$ -axis as  $\cos\theta=x/R$ . Equating the embedded traction and the area over, which it acts with the net bearing capacity load yields  $q_u=NS_u=F/\pi a^2$  or  $F=\pi a^2 NS_u$ . Substituting this into Equation (27) and setting the pore pressure parameters  $B=1$  and  $A_f=0$  yields the undrained change in pore pressure as  $p^u=B\Delta\sigma_m$  or

$$p^u = -\frac{NS_u a^2}{4 R^2} \cos\theta = -\frac{NS_u a^2}{4 R^2} \frac{x}{R} \quad (28)$$

and in dimensionless pressure by pre-multiplying as  $P^u_D = m_v p^u$ . Noting again that volume compressibility, bulk modulus and shear modulus are related as  $m_v=1/K=1/fG$  yields

$$P^u_D = -\frac{N S_u x_D}{4f G R_D^3} \quad (29)$$

This undrained pressure field may be incorporated into the model as an equivalent continuous source through Equation (5). In an analogous manner, the influence of pore pressures generated by shearing may be accommodated where the full expression is  $p^u=B\Delta\sigma_m+BA(\Delta\sigma_1-\Delta\sigma_3)$  and equivalently for the dimensionless form of Equation (29) as

$$P^u_D = -B \frac{N S_u x_D}{4f G R_D^3} - BA \frac{3N S_u}{4f G R_D^5} \max \text{diff} [x_D^3; x_D r_D^2; 0] \quad (30)$$

where  $\max \text{diff}$  represents the maximum span of the three orthogonal stress components as the deviatoric stress.

3.2.2. Partially drained solution. Where the tip geometry is represented by a spherical ball, and the trailing penetrometer shaft is of insignificant diameter relative to this sphere, the local boundary

condition is also given by Equation (25). However, for both the ball geometry, the face angle,  $\theta$ , changes with location around the penetrometer tip. For a sphere of radius,  $a$ , centered at  $(x, r) = (0, 0)$  and with the positive  $x$  – axis aligned upward (Figure 2), the surface is identified parametrically as  $(x, r) = (a \cos \theta, a \sin \theta)$ . Here,  $\theta$ , is the angle relative to the positive  $x$  – axis and also represents the local inclination of the penetrometer face, relative to the  $r$  – axis (Figure 2). Substituting  $x = a \cos \theta$  into Equation (25) yields the equivalent non-dimensional flux at the penetrometer face as

$$Q_D^{b \text{ CPT-Ball}} = \frac{q}{U} = \sin \theta = -\frac{x}{a} = -x_D \quad (31)$$

and is defined as positive for flow outward from the penetrometer face and into the moving medium.

*3.2.3. Asymptotic pore pressure magnitudes.* Again, asymptotic magnitudes are available for the source solutions in both the undrained and partially drained cases. For the undrained case, Equation (29) at  $R_D = 1$  yields

$$P_D = -2.14 \frac{Su}{G} x_D \quad (32)$$

and for  $m_v \rightarrow 0$ , the partially drained solution asymptotes to  $P_D = -x_D/2$ . The variation of these limiting magnitudes with various  $G/Su$  is reported in Table I.

*3.2.4. Results and discussion.* The undrained pore pressure field is used as a source for the soil transport model is illustrated in Figure 8(a). This pseudo-elastic pressure field is positive below the probe and negative above. The streaklines show the proximity of the flow field to the ball face. The resulting steady distribution of pore fluid pressure is shown in Figure 8(b)–(e) for penetration rates of 0.1–100. These results are not specific to a particular rigidity ratio but are identical for a full range of ratios. This artifact is because the volume of the failure zone does not scale with rigidity, unlike for the cavity expansion solution where the failure zone scales with  $(G/Su)^{1/3}$ . The undrained response is almost fully developed at  $U_D \sim 10$  and is absent at  $U_D \sim 0.1$ , again spanning about two orders of magnitude. Because of the nature of the undrained solution, the pore pressure field is antisymmetric about a horizontal plane through the center of the ball tip.

The normalized induced pressures at pressure recording ports at the ball tip, equator (springline) and shaft are shown in Figure 9. Because the magnitude of the induced pore pressure scales directly with  $G/Su$ , but its distribution does not change (dissimilar from the cavity expansion solution where the failure zone extends radially with increasing  $G/Su$ ), the results are the same for all ratios  $G/Su$ . Drivage-induced pressures are positive at the ball tip location but negative elsewhere, including the equatorial position and on the shaft. Also, a curiosity is that at intermediate penetration rates, the tip-generated pore pressures show a net reduction in pressure.

The absolute pressure magnitudes are shown in Figure 10(a) and (b). These are normalized with respect to bulk modulus in Figure 10(a) and with respect to undrained shear strength in Figure 10(b). These identify an asymptotic magnitude of dimensionless pore pressure for large penetration rates as  $(p - p_s)/Su \sim 3$ . Again, the pore pressures predicted for face injection provide an upper bound to pressures predicted from the approximate solution for the ball penetrometer.

#### 4. DATA ANALYSIS

Data from a series of carefully controlled centrifuge penetrometer experiments with a miniature CPT [29] are shown in Figure 11(a). Experiments in fabricated samples offer the potential for both applying unusual constraint on material and boundary conditions and in exercising soil behavior under appropriate stress paths [29, 30]. The results are from multiple penetrations at varied penetration rates but, for a single sample, are shown in Figure 11(a), accessing a full range of dimensionless penetration rates. At low penetration rates, the data closely match the response for  $G/Su = 1000$ , depart slightly as penetration rates increase but converge to the upper limit response as

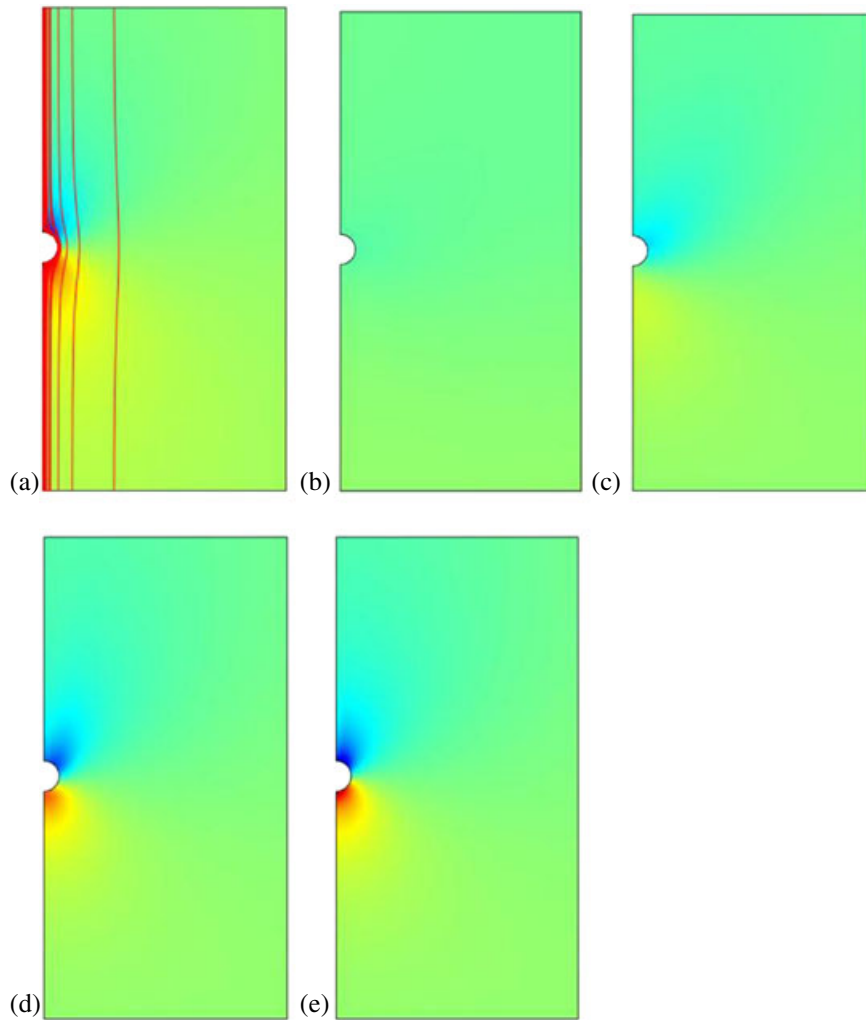


Figure 8. Contour plots of equivalent pore pressures around a ball penetrometer. Plots are for  $P_D U_D = (p - p_s)/K$  and at uniform color key for contours with hot representing highest pressure ( $P_D U_D = (p - p_s)/K = 1.97.7 \times 10^{-3}$ ). Individual frames are for (a) prescribed pressure field for undrained condition and streaklines for solid flowfield and for  $U_D = Ua/C_v$  magnitudes of (b) 0.1, (c) 1, (d) 10 and (e) 100, all for  $G/Su = 1000$  (which is representative of all  $G/Su$ ).

$U_D$  increases above 100. Although not perfect, the fit identifies the correct range for the partially drained response, anchoring the lower and upper limits.

These same data [29] may be transformed and plotted as normalized pressure  $(p - p_s)/\sigma'_{v0} = B_q Q_t$  versus dimensionless permeability  $K_D = 4\sigma'_{v0} m_v / U_D$  rather than against penetration rate. These data yield magnitudes of peak pressure magnitudes  $(p - p_s)/\sigma'_{v0} = B_q Q_t$  in excess of unity, as shown. The data also follow the predicted response for the distributed source solution and remains offset from the face injection solution, which neglects the effects of fluid storage around the cone tip. From the nature of these data, this effect appears important.

## 5. CONCLUSIONS

Approximate models have been presented to represent the evolution of pore pressures in the process zone around standard conical and ball penetrometers. The models use the flow-field developed by an

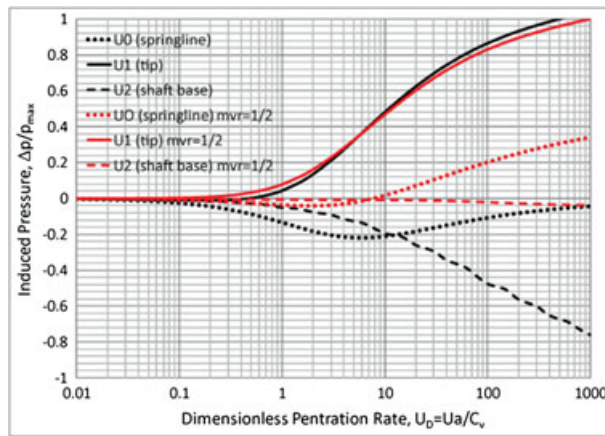


Figure 9. Variation of normalized pore pressures with insertion rate for a ball penetrometer. All pressure normalized relative to peak induce pressure at tip location for  $U_D = 1000$ . Notation  $mvr = 1/2$  represents compressibility in decompression and recompression half that in virgin compression.

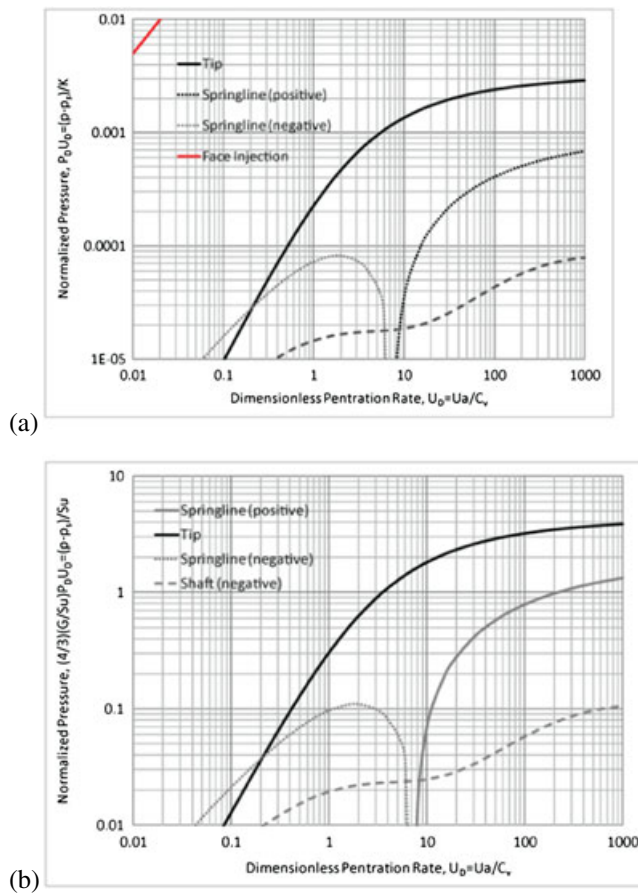


Figure 10. Variation in normalized pressures with dimensionless insertion rate ( $U_D$ ) for the ball penetrometer. Induced pore fluid pressures are normalized with respect to (a) bulk modulus as  $(p - p_s)/K = 3(p - p_s)/4G$  and (b) undrained shear strength as  $(p - p_s)/Su$  for soil compressibility in decompression and in recompression half that in virgin compression.

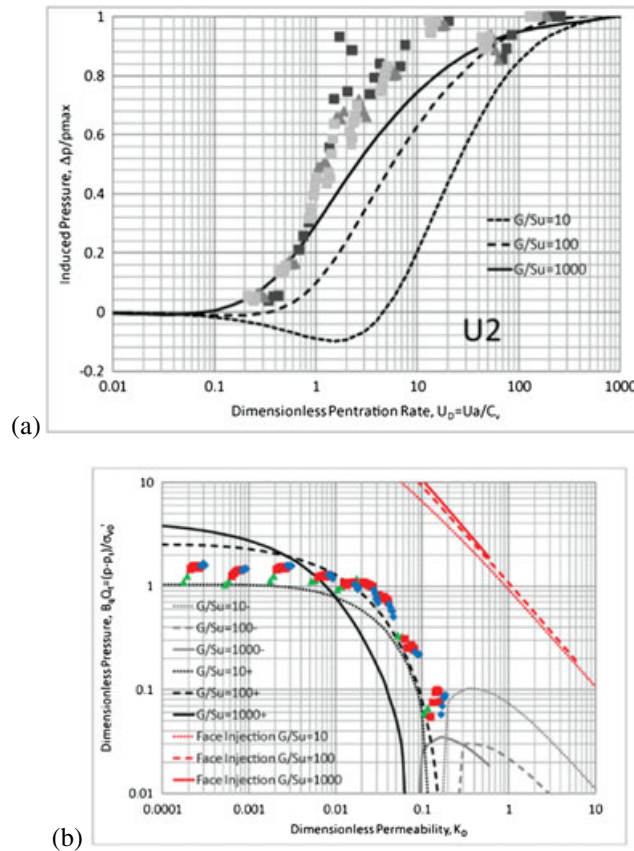


Figure 11. (a) Variation of normalized pore pressures with insertion rate for a standard penetrometer for U2 (shoulder) positions.  $G/S_u$  in the range 10, 100 and 1000, with overprinted centrifuge data for a miniature penetrometer [29]. (b) Same data plotted as  $(p - p_s)/\sigma'_{v0} = B_q Q_t$  versus  $K_D = 4\sigma'_{v0}m_v/U_D$  against model data. All pore pressure data points are positive. Note vertical asymptotes are an artifact of plotting a trace of positive-turning-to-negative pressures on a log scale.

incompressible soil–fluid mixture adjacent to the tip to define the trajectories of the migrating soil, relative to the penetrometer. A stress-decoupled solution for pressure diffusion in an advecting solid field is used to define the evolution of the fluid field adjacent to the tip. The source term for this pressure diffusion system is either from (i) a prescribed zone of failure around the tip, which satisfies stress equilibrium but not fluid continuity; or from (ii) injection of fluid through the face of the penetrometer, which satisfies fluid continuity but not stress equilibrium.

Although not rigorously coupled to deformation, this approximate analysis is able to replicate the principal features of rate effects observed in well-controlled laboratory and field experiments.

Approaches accommodating failure around the probe replicate observations most closely. For the standard penetrometer, the transition from drained to undrained behavior occurs over about two orders of magnitude in penetration rate for pore pressures recorded at the tip (U1) and about two-and-a-half orders of magnitude for the shoulder (U2). This response is strongly influenced by the rigidity of the soil and slightly influenced by the model linking induced total stresses to pore pressures. For the ball penetrometer, the transition from drained to undrained behavior also transits two-and-a-half orders of magnitude in penetration rate, although it is offset to higher dimensionless penetration rates than for standard penetration.

Approaches including only face injection are known to be incapable of replicating response where penetration is undrained, although limits may be placed in the range of their applicability [23]. For partial drainage, these approaches have been shown acceptable and capable of estimating magnitudes of permeability from on-the-fly measurements of induced pore pressures [31]. Face

injection provides a reasonable upper limit to induced pore pressures at low penetration rates and for low ratios of  $G/Su$  (Figure 7) but deviates at high penetration rates when penetration is undrained.

### NOTATION

Symbol	Description (Units)
$a$	Cone radius and normalizing parameter (L)
$A_f$	Skempton pore pressure parameter (-)
$B_q$	Dimensionless U2 cone pore pressure magnitude ( $ML^{-1}T^{-2}$ )
$C_v$	Coefficient of consolidation ( $M^2T^{-1}$ )
$G$	Drained shear modulus ( $ML^{-1}T^{-2}$ )
$k$	Permeability ( $L^2$ )
$K$	Drained bulk modulus $K = 1/m_v$ ( $ML^{-1}T^{-2}$ )
$l, l_D$	Length of taper on penetrometer tip, dimensionless length (L)
$m_v$	Bulk coefficient of compressibility ( $M^{-1}LT^2$ )
$p, p^u, p_s$	Pore fluid pressure, undrained pore fluid pressure, and in situ pore fluid pressure ( $ML^{-1}T^{-2}$ )
$P_D, P_D^U$	Dimensionless pore fluid pressure, dimensionless undrained pore fluid pressure (-)
$q_i$	Darcy flux or fluid velocity ( $LT^{-1}$ )
$Q, Q_D, Q_D^b$	Volumetric flux, dimensionless volumetric flux, and dimensionless boundary flux ( $T^{-1}, -, -$ )
$Q_t$	Dimensionless cone end bearing (-)
$r = x_2$	Radial ordinate (L)
$R, R_{max}, R_D, R_{Dmax}$	Radius from origin ( $\sqrt{x_1^2 + r^2}$ ), extent of plastic zone for cavity expansion, dimensionless radius, dimensionless radius of plastic zone (L, L, -, -)
$Su$	Undrained shear strength ( $ML^{-1}T^{-2}$ )
$t, t_D$	Time, dimensionless time (T)
$U, U_D$	Penetrometer velocity in $-x_1$ direction, dimensionless velocity ( $LT^{-1}$ )
$v_i$	Soil velocity in $+x_1$ direction ( $LT^{-1}$ )
$x_i, x_D$	Coordinates, dimensionless coordinates (L, -)
$\epsilon_v$	Volumetric strain (-)
$\mu, \mu_s$	Viscosity of water, and soil ( $ML^{-1}T^{-1}$ )
$\nu$	Poisson ratio of soil (-)
$\theta$	Cone semi-interapical angle (-)
$\rho_s$	Soil bulk density ( $ML^{-3}$ )
$(\sigma_{11}, \sigma_{22}, \sigma_{33}), (\sigma_x, \sigma_r, \sigma_\theta)$	Stresses ( $ML^{-1}T^{-2}$ )

### ACKNOWLEDGEMENTS

This work is a partial result of support from the US National Science Foundation under grants CMS-0409002 and a supplement under the NSF-IREE Program. This support is gratefully acknowledged. Some concepts of this work evolved from discussions with Mark Randolph during a visit to UWA—this generosity is similarly acknowledged.

### REFERENCES

1. Lunne T, Robertson PK, Powell JJM. *Cone Penetration Testing in Geotechnical Practice*. Blackie Academic and Professional, 1997.
2. Robertson PK, Campanella RG, Gillespie D, Greig J. Use of piezometer cone data. *Proc. ASCE Spec. Conf. In Situ '86. Use of In Sit Tests in Geotechnical Engineering*, Blacksburg, 1986; 1263–1280.
3. Ladanyi B. Expansion of a cavity in a saturated clay medium. *Journal of the Soil Mechanics and Foundation Engineering Division, ASCE* 1963; **89**(4):127–161.
4. Randolph MF, Wroth CP. Analytical Solution for the Consolidation around a Driven Pile. *International Journal for Numerical and Analytical Methods in Geomechanics* 1979; **3**(3):217–229.

5. Vesic AS. Expansion of cavities in infinite soil mass. *Journal of the Soil Mechanics and Foundations Division* 1972; **98**:265–290.
6. Chen BS-Y, Mayne PW. Profiling the overconsolidation ratio of clays by piezocone test. In *Report No. GIT-CEE/GEO-94-1*, National Science Foundation (ed.). Georgia Institute of Technology: Atlanta, 1994; 280.
7. Torstensson BA. The pore pressure probe. *Nordiske Geotekniske Mote, Oslo Paper 34*, 1977; 34.1–34.15.
8. Levadoux JN, Baligh MM. Consolidation after undrained piezocone penetration. I: Prediction. *Journal of Geotechnical Engineering* 1986; **112**(7):707–725.
9. Robertson PK, Sully JP, Woeller DJ, Lunne T, Powell JJM, Gillespie DG. Estimating coefficient of consolidation from piezocone tests. *Canadian Geotechnical Journal* 1992; **29**(4):539–550.
10. Baligh MM, Scott RF. Analysis of deep wedge penetration in clay. *Geotechnique* 1976; **26**(1):185–208.
11. Drescher A, Kang M. Kinematic approach to limit load for steady penetration in rigid-plastic soils. *Geotechnique* 1987; **37**(3):233–246.
12. Acar YB, Tumay MT. Strain field around cones in steady penetration. *Journal of Geotechnical Engineering* 1986; **112**(2):207–213.
13. Tumay MT, Acar YB, Cekirge MH, Ramesh N. Flow field around cone in steady penetration. *Journal of the Geotechnical Engineering Division, ASCE* 1985; **111**(2):193–204.
14. Biot MA, Willis DG. The elastic coefficients of the theory of consolidation. *Journal of Applied Mechanics* 1957; **24**:594–601.
15. Skempton AW. The pore pressure coefficients A and B. *Geotechnique* 1954; **4**:143–147.
16. Baligh MM. Strain path method. *Journal of the Geotechnical Engineering Division, ASCE* 1985; **111**(9):1108–1136.
17. Baligh MM, Levadoux JN. Consolidation after undrained piezocone penetration. II: Interpretation. *Journal of Geotechnical Engineering* 1986; **112**(7):727–745.
18. Teh C, Houlby G. An analytical study of the cone penetration test in clay. *Geotechnique* 1991; **41**:17–34.
19. Elsworth D. Dislocation analysis of penetration in saturated porous media. *Journal of Engineering Mechanics* 1991; **117**(2):391–408.
20. Elsworth D. Pore pressure response due to penetration through layered media. *International Journal for Numerical and Analytical Methods in Geomechanics* 1992; **16**:45–64.
21. Elsworth D. Indentation of a sharp penetrometer in a poroelastic medium. *International Journal of Solids and Structures* 1998; **35**(34–35):4895–4904.
22. Elsworth D, Lee DS. Permeability determination from on-the-fly piezocone sounding. *Journal of Geotechnical and Geoenvironmental Engineering* 2005; **131**(5):643–653.
23. Elsworth D, Lee DS. Limits in determining permeability from on-the-fly uCPT soundings. *Geotechnique* 2007; **131**:30.
24. Fitzgerald M, Elsworth D. Evolution of the pore-pressure field around a moving conical penetrometer of finite size. *Journal of Engineering Mechanics-ASCE* 2010; **136**(3):263–272. DOI:10.1061/(ASCE)0733-9399(2010)136:3(263).
25. Elsworth D, Lee DS, Hryciw R, Shin S. Pore pressure response following undrained uCPT sounding in a dilating soil. *Journal of Geotechnical and Geoenvironmental Engineering* 2006; **132**(11):1485–1495.
26. Einav I, Randolph MF. Combining upper bound and strain path methods for evaluating penetration resistance. *International Journal for Numerical Methods in Engineering* 2005; **63**(14):1991–2016.
27. Randolph MF, Houlby GT. The Limiting Pressure on a Circular Pile Loaded Laterally in Cohesive Soil. *Geotechnique* 1984; **34**(4):613–623.
28. Randolph MF. Personal communication, 2007.
29. Randolph MF, Hope S. Effect of cone velocity on cone resistance and excess pore pressure. *IS Osaka - Engineering Practice and Performance of Soft Deposits*, Osaka, Japan, 2004; 147–152.
30. House AR, Oliveira JRMS, Randolph MF. Evaluating the coefficient of consolidation using penetration tests. *International Journal of Physical Modelling in Geotechnics* 2001; **1**(3):17–25.
31. Lee DS, Elsworth D, Hryciw R. Hydraulic Conductivity Measurements from on-the-fly uCPT sounding and from VisCPT. *Journal of Geotechnical and Geoenvironmental Engineering* 2008; **134**(12):1720–1729.